Hindawi
International Journal of Aerospace Engineering
Volume 2019, Article ID 6917393, 8 pages
https://doi.org/10.1155/2019/6917393

Research Article

A L_1 Adaptive Control Scheme for UAV Carrier Landing Using Nonlinear Dynamic Inversion

Ke Lu [1,2] **and Chunsheng Liu** [1]

[1] *College of Automation Engineering, Nanjing University of Aeronautics and Astronautics, Nanjing, Jiangsu 210016, China*
[2] *Science & Technology on Rotorcraft Aeromechanics Laboratory, China Helicopter Research and Development Institute, Jingdezhen, Jiangxi, 333001, China*

Correspondence should be addressed to Ke Lu; looknuaa@163.com

Received 31 October 2018; Revised 20 January 2019; Accepted 25 February 2019; Published 2 May 2019

Academic Editor: André Cavalieri

This paper presents a L_1 adaptive controller augmenting a dynamic inversion controller for UAV (unmanned aerial vehicle) carrier landing. A three axis and a power compensator NDI (nonlinear dynamic inversion) controller serves as the baseline controller for this architecture. The inner-loop command inputs are roll-rate, pitch-rate, yaw-rate, and thrust commands. The outer-loop command inputs come from the guidance law to correct the glide slope. However, imperfect model inversion and nonaccurate aerodynamic data may cause degradation of performance and may lead to the failure of the carrier landing. The L_1 adaptive controller is designed as augmentation controller to account for matched and unmatched system uncertainties. The performance of the controller is examined through a Monte Carlo simulation which shows the effectiveness of the developed L_1 adaptive control scheme based on nonlinear dynamic inversion.

1. Introduction

Aircraft carrier landings have been regarded as one of the most challenging phases of flight due to the extremely tight space available for touchdown on the flight deck of an aircraft carrier. The pilot must aim for a single spot on the flight deck with a very small margin for error [1]. The area used to land on the deck is very small, which is only about 55 feet wide and 40 feet long. A small deviation from the desired landing box may lead to crashing into other aircraft on the flight deck. The problem of autonomous carrier landing of UAV is highly challenging due to wind gust disturbances and ship motion under high sea states [2]. However, carrier flight operations are necessary for the support of combat operations and must take place whenever they are needed. With consideration of all of the effects, developing a system which automates the carrier landing process is extremely important and will increase the design difficulty of controller [3].

While the topic of automated carrier landing has been studied for several decades, most researchers have focused on linear control methods. H-dot and glide-slope feedback are used as their bases which are found in Ref. [4–6]. However, with air turbulence added, the landing performances of these controllers were degraded [5]. As carrier landing systems are inherently nonlinear, nonlinear control schemes should be the next logical step with the development of computer capability. In Ref. [7], Steinberg expanded his investigation to the application of a fuzzy logic carrier landing system. What he cared about was the ability of the controller to adapt to changing conditions, and the initial results were promising. In Ref. [8], Steinberg and Page compared the baseline performances of several different nonlinear control schemes applied to automated carrier landing. It showed that the nonlinear control may be a very good choice for future carrier landing system. In Ref. [9], a fuzzy-logic-based approach was used to design an autonomous landing system for unmanned aerial vehicles. In Ref. [10], preview control for unmanned aerial vehicle carrier landing was presented. In Ref. [11], active disturbance rejection control was used for unmanned aerial vehicle carrier landing. These nonlinear control methods proved useful in this application. Denison applied nonlinear dynamic inversion to design a carrier

landing system for unmanned combat aerial vehicles considering turbulence [12]. The performance of the system was evaluated using Monte-Carlo simulations. However, after adding wind and sea state turbulence, the controller performance was degraded. Although nonlinear dynamic inversion could eliminate the need for extensive gain scheduling, however, since the system parameters are not exactly known and the plant inversion is not accurate, dynamic inversion controller may possess performance degradation. In order to solve this problem, in Ref. [13], online neural networks were used to compensate plant inversion error. Sliding mode variable structure control could be used to enhance the system robustness, but the chatter problem is not very acceptable [14]. Another widely used method is the linear robust controller [15, 16]. However, a high-order robust controller is required, such as a fourteen-order controller to ensure the flying control system robustness for X-38 [17].

L_1 adaptive control algorithm is a recently developed adaptive control methodology. The key feature of L_1 adaptive control architecture is its fast and robust adaptation, which does not interact with the trade-off between performance and robustness [18]. It was developed with aerospace control in mind and has been found to be suitable for flying applications [19, 20].

In this paper, nonlinear dynamic inversion based controller is designed for carrier landing flight control system. Then L_1 adaptive control algorithm is used to augment the baseline controller. The effects of the adaptive element on the flight control system are demonstrated with Monte Carlo simulations.

2. UAV Flight Dynamics Model and Carrier Landing Environment

In this section, a nonlinear UAV flight dynamics model is developed. Then, the carrier landing environment is described.

2.1. UAV Flight Dynamics Model. The aircraft which was used for this study was the Joint Unmanned Combat Air System (J-UCAS) Equivalent Model (EQ model) developed by the Air Force Research Laboratory (AFRL) [21]. The EQ model has three sets of control surfaces: flaps for pitch control, elevons for roll control, and clamshells for yaw control. The physical parameters for the aircraft are summarized in Table 1.

The simulation uses the standard equations of motion and kinematic relations found in a variety of standard references on flight dynamics.

$$\dot{\mathbf{X}} = \mathbf{F}(\mathbf{X}, \mathbf{U}, \boldsymbol{\sigma}), \tag{1}$$

where $\mathbf{F}(.) \in \mathrm{R}^{12\times 1}$ denotes a vector of nonlinear algebraic equations involving $\mathbf{X}$, $\mathbf{U}$, and $\boldsymbol{\sigma}$. The state variables are given in the form of a vector $\mathbf{X} \in \mathrm{R}^{12\times 1}$; $\mathbf{U} = [\delta_e, \delta_f, \delta_c, \delta_t]$ denotes a vector constituting the control inputs; $\boldsymbol{\sigma}$ is unmodeled nonlinearity dynamics.

2.2. Aircraft Carrier Model and Wind Turbulence Model. The Nimitz-class carrier is employed in this paper. There are 4 wires spaced 40 feet apart for aircraft landing. The detailed parameters can be found in Ref. [12]. The aircraft carrier motion is composed of a forward motion with constant velocity and perturbations caused by sea states. The perturbations are composed of rotational degrees and translational degrees of freedom. The rotational degrees of freedom are termed roll and pitch. In the translational degrees of freedom, up and down motion is called heave, forward to aft motion is called surge, and port to starboard motion is called sway [12]. The perturbations are modeled as sinusoidal waves using the information provided in Table 2 [12, 22]. Sea state 0 refers to calm seas and the values are all zero, and sea state 6 is extremely heavy seas.

A large source of touchdown error is the turbulent air environment found in the approach path [4]. The wind turbulence model is composed of the free atmospheric turbulence and ship burble. The burble is the wind pattern found immediately behind the carrier fantail, which consists of a steady component, an unsteady component, and a periodic component [22].

Table 1: Summary of EQ model physical parameters.

Parameter	Value
Weight	1.20×10^4 kg
Wing area	75.12 m^2
Mean aerodynamic chord	5.68 m
Wing span	16.67 m
Aspect ratio	3.70
I_{xx}	6.52×10^4 kg·m^2
I_{yy}	4.29×10^4 kg·m^2
I_{zz}	1.33×10^5 kg·m^2
$I_{xz}\, I_{xy}\, I_{zy}$	0.00 kg·m^2

Table 2: Summary of sea state perturbations.

Sea state	Perturbation	Amplitude	Frequency
4	Roll	0.6223 deg	0.2856 rad/sec
	Pitch	0.5162 deg	0.5236 rad/sec
	Surge	0.9546 ft	0.3307 rad/sec
	Sway	1.4142 ft	0.3307 rad/sec
	Heave	2.2274 ft	0.3491 rad/sec
5	Roll	0.9829 deg	0.2856 rad/sec
	Pitch	0.8202 deg	0.5236 rad/sec
	Surge	1.5203 ft	0.3307 rad/sec
	Sway	2.2627 ft	0.3307 rad/sec
	Heave	3.5638 ft	0.3491 rad/sec
6	Roll	1.4425 deg	0.2856 rad/sec
	Pitch	1.2374 deg	0.5236 rad/sec
	Surge	2.2840 ft	0.3307 rad/sec
	Sway	3.3941 ft	0.3307 rad/sec
	Heave	5.3528 ft	0.3491 rad/sec

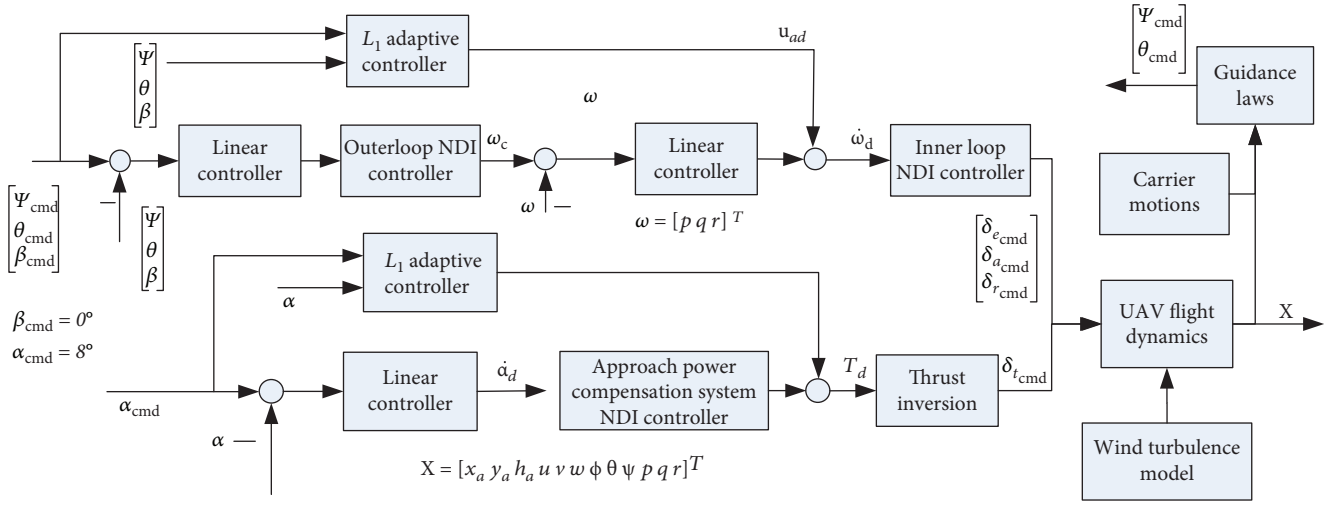

Figure 1: Flight control system block diagram.

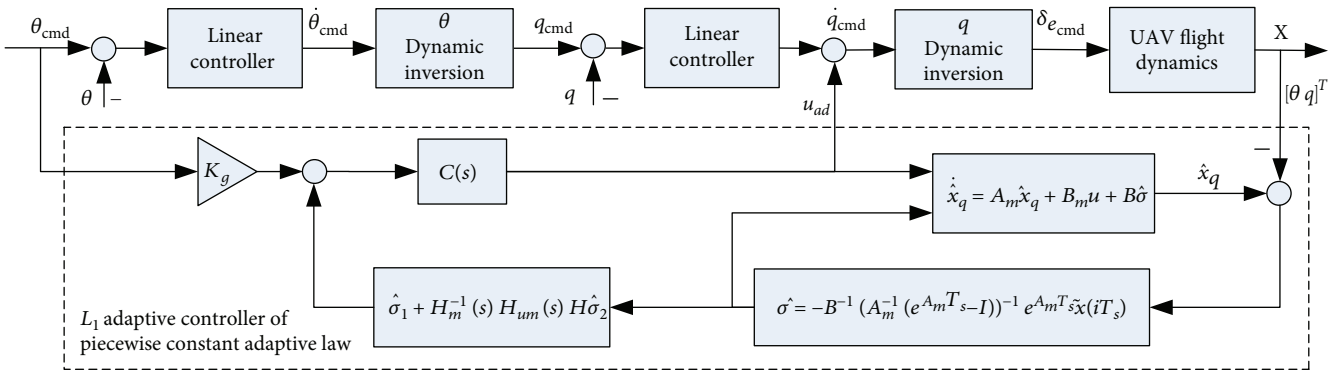

Figure 2: Block diagram of L_1 adaptive controller of piecewise constant adaptive law for pitch channel.

The wind turbulence model is given by

$$\begin{cases} U_g = U_1 + U_2 + U_3 + U_4, \\ V_g = V_1 + V_4, \\ W_g = W_1 + W_2 + W_3 + W_4, \end{cases} \tag{2}$$

where U_1, V_1, and W_1 represent free atmospheric turbulence; U_2 and W_2 represent the steady component of burble turbulence; U_3 and W_3 represent the periodic component of burble turbulence; U_4, V_4, and W_4 represent random component of burble turbulence. The periodic component could be ignored, as it is due to the slow pitch periodic motion of carrier. The random component of burble and free atmospheric turbulence are modeled using Dryden turbulence [12]. In this study, the Dryden wind turbulence model uses the Dryden spectral representation by passing band-limited white noise through appropriate forming filters to meet the MIL-HDBK-1797B, while the steady component is essentially a shift in all components of the turbulence, which causes a 6 ft drop below the glide slope and consequent touchdown 125 ft short of the ideal touchdown point [4].

3. The Controller Design

In this section, a L_1 adaptive augmented dynamic inversion controller for UAV carrier landing is designed. In this study, the command inputs for the controller are provided by the guidance system. The guidance system generate the yaw angle and pitch angle commands which can be found in Ref. [12]. The side-slip angle command is always zero, and the angle of attack command depends on Approach Power Compensation System. The Approach Power Compensation System automatically controls thrust to maintain a reference angle of attack during the carrier approach, thus effectively controlling the flight path angle through pitch angle [5, 23]. The baseline controller is a full nonlinear dynamic inversion controller based on large part of Ref. [24] and Ref. [12]. An inner-loop controller, designed by dynamic inversion, is used to linearize the UAV dynamics. This inner-loop controller lacks guaranteed robustness to uncertainties in the flight dynamics model. This would cause degradation of NDI controller performance and even lead to the failure of the carrier landing. To address robustness to model uncertainties, a L_1 adaptive controller is designed as augmentation controller. The complete architecture is presented in Figure 1.

3.1. Baseline Controller: Nonlinear Dynamic Inversion. Nonlinear dynamic inversion is a technique in which feedback is used to linearize the system to be controlled and to provide desired dynamic [15, 24]. The inner loop controller is used to control the angular accelerations and thrust of the aircraft. Thus, a simple first-order equation was added for thrust control [12].

$$\dot{T} = \frac{1}{\tau}(\delta_t T_{\max} - T), \tag{3}$$

where τ is the engine time constant and $T_{\max}$ is the maximum at the given flight condition.

The inner-loop dynamics are presented below:

$$\dot{\mathbf{X}}_{\text{in}} = \mathbf{F}_{\text{in}}(\mathbf{X})\mathbf{X}_{\text{in}} + \mathbf{G}_{\text{in}}(\mathbf{X})\mathbf{U}_{\text{in}}, \tag{4}$$

where $\mathbf{X}_{\text{in}} = [p\ q\ r\ T]^{\text{T}}$; $\mathbf{F}_{\text{in}}(.) \in \text{R}^{4\times1}$ and $\mathbf{G}_{\text{in}}(.) \in \text{R}^{4\times1}$ are vectors of nonlinear algebraic equations.

With the pseudocontrol signal $\dot{\mathbf{X}}_{\text{ind}}$, the general nonlinear dynamic inversion control law is given by

$$\mathbf{U}_{\text{in}} = \widehat{\mathbf{G}}_{\text{in}}^{-1}\left(\dot{\mathbf{X}}_{\text{ind}} - \widehat{\mathbf{F}}_{\text{in}}(\mathbf{X})\mathbf{X}_{\text{in}}\right), \tag{5}$$

where the over-hats have been used to denote that parameters are estimated, which are provided through look-up tables in a real-time operation.

Inserting equation (5) into equation (4) leads to the following equation:

$$\dot{\mathbf{X}}_{\text{in}} = \mathbf{F}_{\text{in}}(\mathbf{X})\mathbf{X}_{\text{in}} - \mathbf{G}_{\text{in}}(\mathbf{X})\widehat{\mathbf{G}}_{\text{in}}^{-1}\widehat{\mathbf{F}}_{\text{in}}(\mathbf{X})\mathbf{X}_{\text{in}} + \mathbf{G}_{\text{in}}(\mathbf{X})\widehat{\mathbf{G}}_{\text{in}}^{-1}\dot{\mathbf{X}}_{\text{ind}}. \tag{6}$$

Equation (6) is the actual closed-loop input/output relation after applying feedback linearization. Moreover, if the estimates in equation (6) are exact, then equation (6) yields an exact linear relation:

$$\dot{\mathbf{X}}_{\text{in}} = \dot{\mathbf{X}}_{\text{ind}}. \tag{7}$$

The out-loop dynamics inversion controller is designed in much the same way as the interloop controller. The out-loop dynamics are presented below:

$$\dot{\mathbf{X}}_{\text{out}} = \mathbf{F}_{\text{out}}(\mathbf{X}_{\text{out}}) + \mathbf{G}_{\text{out}}(\mathbf{X}_{\text{out}})\mathbf{X}_{\text{in}}, \tag{8}$$

where $\mathbf{X}_{\text{out}} = [\theta \quad \psi \quad \beta \quad \alpha]^{\text{T}}$; $\mathbf{F}_{\text{out}}(.) \in \text{R}^{4\times1}$ and $\mathbf{G}_{\text{out}}(.) \in \text{R}^{4\times1}$ are vectors of nonlinear algebraic equations.

With the pseudocontrol signal $\dot{\mathbf{X}}_{\text{outd}}$, the general nonlinear dynamic inversion control law is given by

$$\mathbf{X}_{\text{inc}} = \widehat{\mathbf{G}}_{\text{out}}^{-1}\left(\dot{\mathbf{X}}_{\text{outd}} - \mathbf{F}_{\text{out}}(\mathbf{X}_{\text{out}})\right). \tag{9}$$

Inserting equation (9) into equation (8) leads to the following equation:

$$\dot{\mathbf{X}}_{\text{out}} = \mathbf{F}_{\text{out}}(\mathbf{X}_{\text{out}}) + \mathbf{G}_{\text{out}}(\mathbf{X}_{\text{out}})\widehat{\mathbf{G}}_{\text{out}}^{-1}\left(\dot{\mathbf{X}}_{\text{outd}} - \mathbf{F}_{\text{out}}(\mathbf{X}_{\text{out}})\right). \tag{10}$$

If the estimates in equation (10) are exact, then equation (10) yields an exact linear relation:

$$\dot{\mathbf{X}}_{\text{out}} = \dot{\mathbf{X}}_{\text{outd}}. \tag{11}$$

3.2. L_1 Adaptive Controller. The NDI-based controller described assumes exact knowledge of the system. However, this is not the case. To address robustness to model uncertainties, a L_1 adaptive controller is designed as augmentation controller to compensate for unmodeled dynamics.

The pitch channel under baseline controller can be written in the form of

$$\begin{aligned}
\dot{x}_q &= -A_m x_q + B_m u_q(t) + f\left(t, x_q(t), z(t)\right),\\
x_q(0) &= x_{q0},\\
\dot{x}_z(t) &= g(t, x_z(t), q),\\
x_z(0) &= x_{z0},\\
z(t) &= g_0(t, x_z(t)),\\
y(t) &= c^T x_q(t),
\end{aligned} \tag{12}$$

where $x_q = [\theta, q]^T$; $A_m \in R^{2\times2}$ is a known real number defining the desired dynamics for the closed-loop system; B_m, c are known constant vectors; $f(t, x_q(t), z(t))$ represents all nonlinearities and further uncertainties of the system. The unmodeled dynamics of the states Z contribute to these uncertainties; $y(t)$ is the system output.

The system (12) can be written in the form

$$\begin{aligned}
\dot{x}_q &= -A_m x_q + B_m\left(u_q(t) + f_1\left(t, x_q(t), z(t)\right)\right) + B_{um} f_2\left(t, x_q(t), z(t)\right),\\
x_q(0) &= x_{q0},\\
\dot{x}_z(t) &= g\left(t, x_z(t), x_q\right),\\
x_z(0) &= x_{z0},\\
z(t) &= g_0(t, x_z(t)),\\
y(t) &= c^T x_q(t),
\end{aligned} \tag{13}$$

where B_{um} is created as the null space of B_m^T while keeping the square matrix $[B_m \quad B_{um}]$ of full rank. $f_1(\cdot)$ represents the matched component of the uncertainties, whereas $B_{um}f_2(\cdot)$ represents the unmatched component.

The system above verifies the following assumptions [25].

Assumption 1 (Boundedness of $f_i(t,0)$). There exists $B_i > 0$, such that $\|f_i(t,0)\|_\infty \le B_i$ holds for $t \ge 0$ and for $i = 1, 2$.

Assumption 2 (Semiglobal Lipschitz condition). For arbitrary $\delta > 0$, there exist positive $K_{1\delta}$, $K_{2\delta}$, such that

$$\|f_i(t,x_1) - f_i(t,x_2)\|_\infty \le K_{i\delta}\|x_1 - x_2\|_\infty, \quad i = 1,2, \tag{14}$$

for all $\|x_j\|_\infty \le \delta$, $j = 1, 2$, uniformly in t.

Assumption 3 (Stability of unmodeled dynamics). The x_z -dynamics are BIBO stable with respect to both initial conditions x_{z0} and input $x(t)$.

In this study, the uncertainties are mainly caused by aerodynamic parameters and the wind disturbance. They are always uniformly bounded and limited in how fast they can change. Thus, these assumptions are reasonable.

3.2.1. Piecewise Constant L_1 Adaptive Controller Design. The structure of the L_1 adaptive augmentation is depicted in Figure 2. In this application a piecewise constant type of L_1 adaptive controller is used as descried in Ref. [25] Section 3.3.

A piecewise constant L_1 adaptive controller is composed of a state predictor, an adaptive law, and a control law.

(1) State predictor

$$\dot{\hat{x}}_q = A_m\hat{x}_q(t) + B_m(u(t) + \hat{\sigma}_1(t)) + B_{um}\hat{\sigma}_2(t) \tag{15}$$

(2) Adaptive law

$$\begin{bmatrix}\hat{\sigma}_1(t)\\ \hat{\sigma}_2(t)\end{bmatrix} = -B^{-1}\Phi^{-1}(T_s)e^{A_mT_s}\left(\hat{x}_q(iT_s) - x_q(iT_s)\right), \tag{16}$$

where $B = [B_m \quad B_{um}]$, $\Phi(T_s) = A_m^{-1}(e^{A_mT_s} - I)$, and T_s is adaptation sampling time

(3) Control law

$$u_{ad}(s) = C(s)\left(k_g r(s) - \hat{\sigma}_1(s) - H_m^{-1}(s)H_{um}(s)\hat{\sigma}_2(s)\right), \tag{17}$$

where $H_m(s) = c^T(sI - A_m)^{-1}B_m$, $H_{um}(s) = c^T(sI - A_m)^{-1}B_{um}$, and $C(s)$ is low-pass filter with $C(0) = 1$

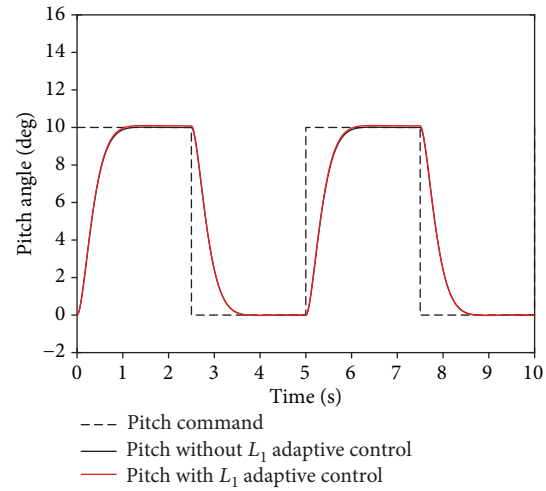

FIGURE 3: Pitch angle capture task without parameter perturbations.

$H_m(s)$ is the reference transfer function from the matched input. $H_{um}(s)$ is the reference transfer function from unmatched input. k_g is set to the steady gain $k_g = -1/(c^TA_m^{-1}B_m)$.

3.2.2. Closed-Loop Reference System and Performance Bounds. We define the closed-loop reference system as [25]

$$\begin{aligned}\dot{x}_{q\text{ref}} &= -A_m x_{q\text{ref}} + B_m\left(u_{q\text{ref}}(t) + f_1\left(t, x_{q\text{ref}}(t), z(t)\right)\right)\\ &\quad + B_{um}f_2\left(t, x_{q\text{ref}}(t), z(t)\right),\\ x_{q\text{ref}}(0) &= x_{q0},\\ u_{q\text{ref}} &= -C(s)\left(\eta_{1\text{ref}}(s) + H_m^{-1}(s)H_{um}(s)\eta_{2\text{ref}}(s) - k_g r(s)\right)\\ y_{\text{ref}}(t) &= c^T x_{q\text{ref}}(t),\end{aligned} \tag{18}$$

where $\eta_{1\text{ref}}(s)$ and $\eta_{2\text{ref}}(s)$ are the Laplace transforms of the signals $\eta_{i\text{ref}}(t) \triangleq f_i(t, x_{q\text{ref}}(t), z(t))$, $i = 1, 2$.

Theorem 1 [25]. *Given the adaptive closed-loop system with the L_1 adaptive controller defined via (15), (16), and (17), subject to the L_1-norm condition, the controlled system (13) will follow the reference system within the following limits:*

$$\begin{aligned}\left\|x_q - x_{q\text{ref}}\right\|_{L_\infty} &\le \gamma_x(T_s),\\ \left\|u_q - u_{q\text{ref}}\right\|_{L_\infty} &\le \gamma_u(T_s),\end{aligned} \tag{19}$$

where γ_x and γ_u are dependent on $f_i(t,x)$ bounds and L_1 controller design parameters, A_m, $C(s)$, and T_s.

Remark 1. As the sampling period T_s goes to zero, the system (13) will follow the reference system (18) arbitrarily

closely. It implies that the performance limitations are consistent with the hardware limitations.

$$\lim_{T_s \to 0} \gamma_x = 0, \quad \lim_{T_s \to 0} \gamma_u = 0, \tag{20}$$

Remark 2. the low-pass filter $C(s)$ defines the trade-off between performance and robustness. Reducing the bandwidth of the filter, the time-delay margin of the system can be increased, while the performance reduced. On the contrary, increasing the bandwidth of the filter leads to improved performance with reduced robustness.

3.2.3. Implementation Details. The desired dynamics for pitch channel is set by a parameter $\omega_\theta = 5$ rad/s, which corresponds to closed-loop reference response bandwidth. The damping parameter is set to 0.9 in this design.

The low-pass filter guarantees that the control signal stays in the low-frequency range even in the presence of fast adaptation. In Ref. [25], the authors suggest that the bandwidth of the filter is not frequencies beyond the control channel bandwidth through to the control signal. On the other hand, the filter bandwidths are related to the corresponding reference system bandwidth. So the filter bandwidths should be higher than the desired system [26].

As presented before, the sampling time T_s has a significant influence on the L_1 adaptive controller with piecewise-constant adaptation law. In Ref. [25], the authors suggest that the sampling time T_s is to choose as low as possible, considering available computing power [25, 27]. After a series of simulations, the following parameters of the L_1 controller were obtained:

$$C(s) = \frac{30}{s + 30}, \quad T_s = 0.005s. \tag{21}$$

4. Simulations

In order to examine the performance of L_1 augmented dynamic inversion controller for UAV carrier landing, three simulation scenarios are considered.

Scenario 1. Pitch angle capture simulation.

In this case, aerodynamic parameters are varied by 20%. Mass and mass inertia properties are varied by 5%. The control effectiveness are varied by 50%. Figure 3 shows the pitch angle tracking performance of the dynamic inversion controller with linear compensation versus its performance with L_1 adaptive controller without parameter perturbations. Without parameter perturbations, performances of both control laws are very similar. However, as the parameter perturbations are added (Figure 4), the performance of the linear controller degrades while the L_1 controller manages to reduce effects of parameter changes to controlled states better.

Scenario 2. UAV carrier landing simple simulation.

In this case, turbulence and sea state effects are not included. The forward speed of UAV is $V_a = 65$ m/s, and the aircraft carrier speed is $V_b = 5$ m/s. Figure 5 depicts the height change during the carrier landing task. Figure 6 depicts the top-down view of the trajectory of both the UAV and the carrier. When the simulation began, the UAV immediately began to turn to intercept the glide path. As it approached the prescribed glide path, it came out approximately on the glide path at the landing heading with little overshoot. It then maintained the prescribed glide path all the way to touchdown. These results show that the controller performs well when turbulence and sea state effects are not included.

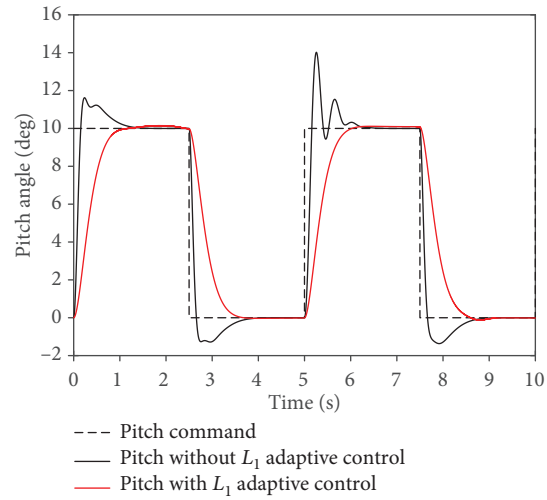

Figure 4: Pitch angle capture task with parameter perturbations.

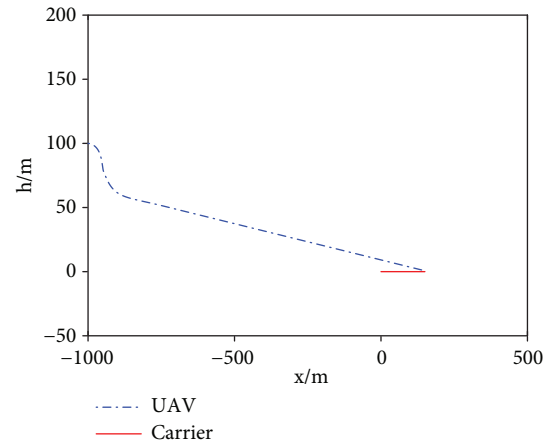

Figure 5: UAV landing trajectory in the vertical plane.

Scenario 3. UAV carrier landing Monte Carlo simulation.

In this case, the performance of the controller is evaluated through a Monte Carlo simulation. In order to compare with Ref [12], the same simulation conditions are set. According to Ref. [22], the simulation results of the total wind disturbance components U_g, V_g, and W_g are shown in Figure 7, and the deck motion under sea state 4 is shown in Figure 8.

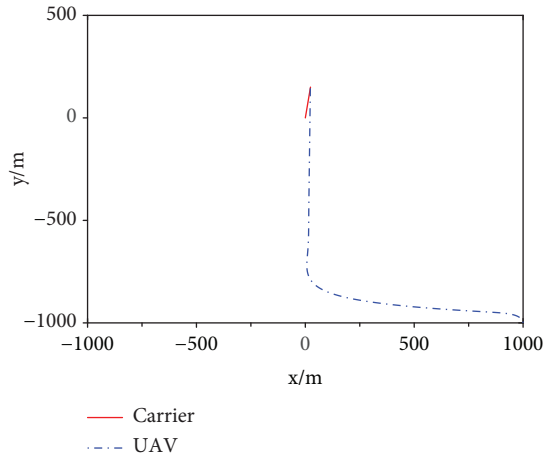

Figure 6: UAV Landing trajectory in the horizontal plane.

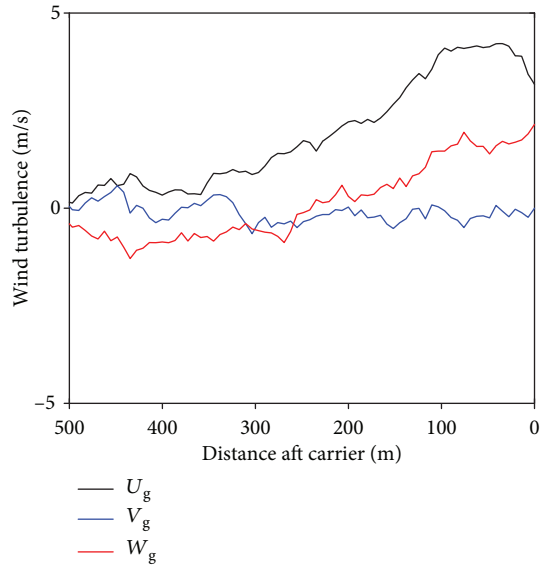

Figure 7: Wind turbulence components.

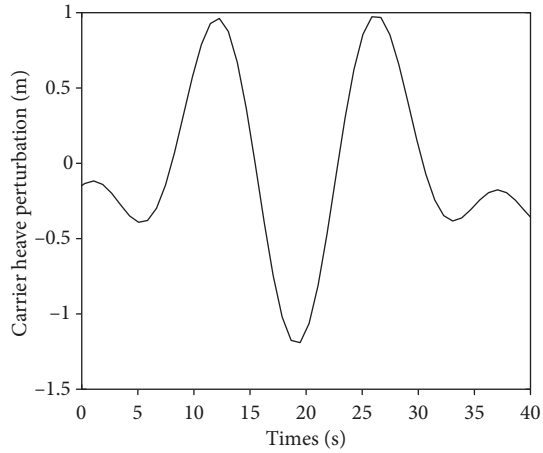

Figure 8: Deck motion under sea state 4.

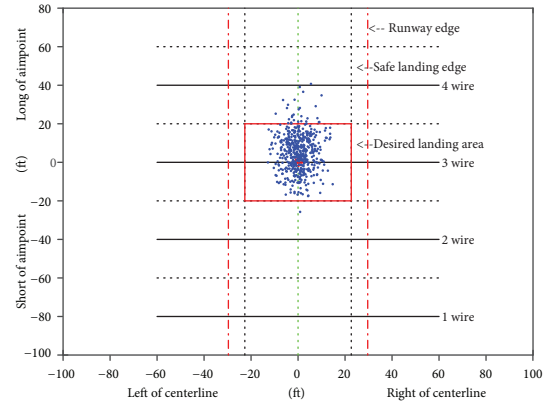

Figure 9: Landing dispersion under NDI controller with L_1 adaptive control augmentation.

The number of 500 Monte Carlo simulation experiments are carried out. In this case, wind turbulence and sea state effects are included. The landing dispersions under NDI baseline controller with linear compensation can be found in Ref [12], while the landing dispersions with L_1 adaptive control augmentation under the same simulation conditions is shown in Figure 9. It can be derived from Ref [12] that the increase in wind turbulence greatly degraded the performance of the controller, as 13 (2.6%) caught the 1 wire, 123 (24.6%) caught the 2 wire, 250 (50.0%) caught the 3 wire, and 114 (22.8%) caught the 4 wire [12]. However, when the L_1 adaptive augmentation was added to the control loop, all 500 simulation runs resulted in a successful trap. Of these, 473 (95%) landed in the desired landing area.

5. Conclusions

In this paper, the design of a nonlinear inversion controller for UAV carrier landing has been developed. Furthermore, it has been explained how to augment this baseline controller with a L_1 adaptive controller. The nonlinear simulation results demonstrate that the baseline controller performs well when the system model is accurate and without wind turbulence. However, when turbulence and sea state effects are included, the landing dispersion under L_1 adaptive augmentation provides significant improvement.

Data Availability

This publication is supported by multiple datasets, which are openly available at locations cited in References.

Conflicts of Interest

The authors declare that there is no conflict of interest regarding the publication of this paper.

Acknowledgments

This work was supported by the Aeronautical Science Foundation of China (Grant No. 20175752045; 2016ZA02001).

References

[1] T. S. Durand and R. J. Wasicko, "Factors influencing glide path control in carrier landing," *Journal of Aircraft*, vol. 4, no. 2, pp. 146–158, 1967.

[2] J. D. Bošković and J. Redding, "An autonomous carrier landing system for unmanned aerial vehicles," in *AIAA Guidance, Navigation, and Control Conference*, Chicago, IL, USA, 2009.

[3] N-UCAS Advanced Development Program, "Unmanned combat air system shipboard interface reference document," Tech. Rep. NA-4580-UCAS-1003, Naval Air Systems Command, 2007.

[4] R. K. Hess, J. M. Urnes, R. F. Moomaw, and R. W. Huff, "H-dot automatic carrier landing system for approach control in turbulence," *Journal of Guidance, Control, and Dynamics*, vol. 4, no. 2, pp. 177–183, 1981.

[5] J. M. Urnes and R. K. Hess, "Development of the F/A-18A automatic carrier landing system," *Journal of Guidance, Control, and Dynamics*, vol. 8, no. 3, pp. 289–295, 1985.

[6] J. Crassidis and D. Mook, "Robust control design of an automatic carrier landing system," in *Astrodynamics Conference*, Hilton Head Island, SC, USA, 1992.

[7] M. Steinberg, "A fuzzy logic based F/A-18 automatic carrier landing system," in *Guidance, Navigation and Control Conference*, Hilton Head Island, SC, USA, 1992.

[8] M. Steinberg and A. Page, "A comparison of neural, fuzzy, evolutionary, and adaptive approaches for carrier landing," in *AIAA Guidance, Navigation, and Control Conference and Exhibit*, Montreal, Canada, 2001.

[9] O. Cetin, S. Kurnaz, and O. Kaynak, "Fuzzy logic based approach to design of autonomous landing system for unmanned aerial vehicles," *Journal of Intelligent & Robotic Systems*, vol. 61, no. 1-4, pp. 239–250, 2011.

[10] Z. Ziyang, M. Kun, and B. A. Kumar, "Automatic carrier landing control for unmanned aerial vehicles based on preview control," *Transactions of Nanjing University of Aeronautics and Astronautics*, vol. 4, pp. 77–83, 2017.

[11] Y. Yu, H. Wang, N. Li, Z. Su, and J. Wu, "Automatic carrier landing system based on active disturbance rejection control with a novel parameters optimizer," *Aerospace Science and Technology*, vol. 69, pp. 149–160, 2017.

[12] N. A. Denison, *Automated carrier landing of an unmanned combat aerial vehicle using dynamic inversion, [M.S. thesis]*, Air Force Institute of Technology, Wright-Patterson AFB, 2007.

[13] M. Chen, Q. Zou, C. Jiang, and Q. Wu, "Dynamical inversion flight control based on neural network disturbance observer," *Control and Decision*, vol. 23, no. 3, pp. 283–287, 2008.

[14] R. Hess and S. Wells, "Sliding mode control applied to reconfigurable flight control design," in *40th AIAA Aerospace Sciences Meeting & Exhibit*, Reno, NV, USA, 2012.

[15] J. Reiner, G. J. Balas, and W. L. Garrard, "Robust dynamic inversion for control of highly maneuverable aircraft," *Journal of Guidance, Control, and Dynamics*, vol. 18, no. 1, pp. 18–24, 1995.

[16] R. J. Adams and S. S. Banda, "Robust flight control design using dynamic inversion and structured singular value synthesis," *IEEE Transactions on Control Systems Technology*, vol. 1, no. 2, pp. 80–92, 1993.

[17] D. Ito, D. Ward, and J. Valasek, "Robust dynamic inversion controller design and analysis for the X-38," in *AIAA Guidance, Navigation, and Control Conference and Exhibit*, Montreal, Canada, 2001.

[18] C. Cao and N. Hovakimyan, "Design and analysis of a novel $\mathscr{L}_1$ adaptive control architecture with guaranteed transient performance," *IEEE Transactions on Automatic Control*, vol. 53, no. 2, pp. 586–591, 2008.

[19] D. Erdos, T. Shima, E. Kharisov, and N. Hovakimyan, "$\mathscr{L}_1$ adaptive control integrated missile autopilot and guidance," in *AIAA Guidance, Navigation, and Control Conference*, Minneapolis, MN, USA, 2012.

[20] H. Lee, S. Snyder, and N. Hovakimyan, "$\mathscr{L}_1$ adaptive control within a flight envelope protection system," *Journal of Guidance, Control, and Dynamics*, vol. 40, no. 4, pp. 1013–1026, 2017.

[21] A. Barfield and J. Hinchman, "An equivalent Model for UAV automated aerial refueling research," in *AIAA Modeling and Simulation Technologies Conference and Exhibit*, San Francisco, CA, USA, 2005.

[22] N-UCAS Advanced Development Program Office, *Unmanned Combat Air System Shipboard Interface Reference Document-NA-4150- USRD -1005*, USA Naval Air Systems Command, 2007.

[23] K. Lu, C. Liu, S. Wu, and C. Li, "Carrier-based aircraft approach power compensator system design based on L_1 adaptive controller," in *2017 36th Chinese Control Conference (CCC)*, pp. 920–923, Dalian, China, 2017.

[24] D. Enns, D. Bugajski, R. Hendrick, and G. Stein, "Dynamic inversion: an evolving methodology for flight control design," *International Journal of Control*, vol. 59, no. 1, pp. 71–91, 1994.

[25] N. Hovakimyan and C. Cao, *$\mathscr{L}_1$ Adaptive Control Theory: Guaranteed Robustness with Fast Adaptation*, Society for Industrial and Applied Mathematics, Philadelphia, PA, USA, 2010.

[26] I. Kaminer, A. Pascoal, E. Xargay, N. Hovakimyan, C. Cao, and V. Dobrokhodov, "Path following for small unmanned aerial vehicles using $\mathscr{L}_1$ adaptive augmentation of commercial autopilots," *Journal of Guidance, Control, and Dynamics*, vol. 33, no. 2, pp. 550–564, 2010.

[27] A. Pettersson, K. Åström, A. Robertsson, and R. Johansson, "Augmenting L1 adaptive control of piecewise constant type to a fighter aircraft. Performance and robustness evaluation for rapid maneuvering," in *AIAA Guidance, Navigation, and Control Conference*, Minneapolis, MN, USA, 2012.